A three-dimensional study on premixed flame propagation in narrow channels considering hydrodynamic and thermodiffusive instabilities

Ziyin Chen, Song Zhao, Bruno Denet, Christophe Almarcha, Pierre Boivin

A three-dimensional study on premixed flame propagation in narrow channels considering hydrodynamic and thermodiffusive instabilities

Ziyin Chen[a,*], Song Zhao[a], Bruno Denet[b], Christophe Almarcha[b], Pierre Boivin[a]

[a]Aix Marseille Univ, CNRS, Centrale Med, M2P2, Marseille, France
[b]Aix Marseille Univ, CNRS, Centrale Med, IRPHE, Marseille, France

Abstract

In numerical studies of quasi-2D problems, such as laminar flame propagation through a slit, the quasi-2D assumption is commonly applied to simplify the problem. However, the impact of the third dimension (in the thickness between walls) can be significant due to strong curvature. The intrinsic Darrieus-Landau instability, the Saffman-Taylor instability, and the thermodiffusive instability lead to curved flame fronts in both the transverse and normal directions and radically change the global flame speed. This study investigates the interaction of these instabilities and their impact on premixed flames freely propagating in narrow channels. Two lean fuel-air mixtures are considered: one with unity Lewis number $Le = 1$ and another with $Le = 0.5$. A single-step Arrhenius-type reaction is used for combustion modeling. Joulin Sivashinsky's model [1], termed the 2D+ model, is implemented to capture the confinement effect due to walls. By comparing 3D Direct Numerical Simulations (DNS) and 2D simulations at unity Le, we find that the 2D+ model accurately reproduces confinement effects for channel width h up to $3.6\delta_T$ (δ_T: thermal flame thickness), extending the validity of Darcy's law.

However, for larger h, interactions between flame curvatures in two directions result in higher flame surface increment and consumption speed. Besides, for 3D cases with $Le = 0.5$, positive curvature regions on the flame front primarily contribute to the global reaction due to the Lewis effect. Statistical studies on flame dynamics between walls in 3D cases are also

*Corresponding author.
Email address: ziyin.chen@univ-amu.fr (Ziyin Chen)

Preprint submitted to Combustion and Flame

conducted, and results show that both the flame surface increment and the Lewis effect on curvature (if $Le = 0.5$) are approximately consistent. 2D simulations for the thickness between walls can predict the acceleration from flame dynamics between walls in the 3D domain for both mixtures.

Keywords: Hydrodynamic instability; Thermodiffusive instability; Confined flow; Premixed flame

---

1. Novelty and Significance Statement

This study is the first three-dimensional study on premixed flame freely propagating in narrow channels considering both hydrodynamic, including Darrieus-Landau (DL) and Saffman-Taylor (ST) instabilities, and thermodiffusive (TD) instabilities. It is also the first to validate the Joulin-Sivashinsky model's ability to incorporate wall confinement effects in 2D simulations across various narrow channel widths through comparisons with 3D direct numerical simulations. This research is significant as it explores the interplay between confinement effect and DL and TD instabilities. It is also significant for its investigation on the interaction of flame curvature in both normal and transverse directions, a phenomenon previously underexplored in confined geometries, and its exploration on the essential impact of flame curvature and the Lewis effect ($Le < 1$) between walls on global flame dynamics at wider channels.

2. Author Contributions

- Z. Chen performed research, analyzed data and wrote the paper
- S. Zhao analyzed data and revised the paper
- B. Denet supervised project and revised the paper
- C. Almarcha supervised project and revised the paper
- P. Boivin supervised project and revised the paper

3. Introduction

Accurately simulating flame regimes in confined environments is crucial for micro-scale combustion devices, where stable combustion is essential for efficiency and safety. Premixed laminar flames exhibit various intrinsic instabilities which profoundly affect flame dynamics: Darrieus-Landau (DL) instability arising from the density contrast across the flame front and yielding a positive growth rate of flame wrinkling and deforming the flame front [2–6]; thermodiffusive (TD) instability which results from the competition between heat and species diffusion across the flame front, and thus could stabilize or destabilize flames depending on the Lewis number and the curvature of the flame front; Saffman-Taylor (ST) instability occurring between two fluids with different viscosity [7] (ST instability is also inherently hydrodynamic [8]). Investigations on the destabilizing/stabilizing of gravity (Rayleigh-Taylor instability) and the interaction between flame dynamics and acoustics have been done in further studies [9–14].

The effects of Darrieus-Landau (DL) and thermodiffusive (TD) instabilities on planar flame stability have been widely studied through theoretical analysis. In the linear regime, perturbations on the flame front either grow or decay exponentially. Matalon et al. [5] developed a dispersion relation to quantify the growth rate of these perturbations, assuming an effective Lewis number close to unity. In contrast, Sivashinsky et al. [2] formulated a model that accommodates a broader range of Lewis numbers but is limited to small density contrasts across the flame front.

In the non-linear regime, theoretical analysis has derived a general nonlinear equation - the Michelson–Sivashinsky equation - based on limiting approximations to describe the unstable flame dynamics [2]. Further theoretical and numerical studies found that the domain size strongly influences equidiffusive premixed flame evolution. Within certain domain sizes (around 40 times flame thickness), the flame stabilizes into a single cusp-like structure pointing toward the burnt gases. In larger domains, continuous merging and splitting of cusps result in unsteady flame dynamics, a phenomenon extensively studied both experimentally and numerically. A well-established configuration for studying this instability is the Hele-Shaw burner, which consists of two parallel plates separated by a narrow channel width h, where premixed flames propagate between the walls. Experimental studies using this setup have provided valuable insights into flame dynamics and have shown strong agreement with theoretical predictions [6, 15].

In confined environments, such as the Hele-Shaw burner, momentum and heat losses at the walls influence hydrodynamic instabilities. Joulin

and Sivashinsky conducted a linear stability analysis on these effects [1]. By modeling the flame as an effective interface and using Euler-Darcy equations for both unburnt and burnt gases, they introduced a viscosity-based exchange coefficient $f \sim \mu/h^2$ (μ[kgm^{-1}s^{-1}]: gas dynamic viscosity) to include the momentum losses into the momentum equation, demonstrating that friction induced pressure gradients, coupled with viscosity contrast, would enhance the Saffman-Taylor instability. Further numerical studies extended the Joulin-Sivashinsky model to the Navier-Stokes equations for reacting flows and performed linear stability analyses [8, 16, 17]. Assuming Poiseuille and isobaric flow, these studies found that momentum losses due to wall friction destabilize the flame and significantly impact its dynamics. Free flame propagation is considered in [8, 16], while the analysis in [1] is with the fresh gases flow moving at the planar flame speed against the flame. Further studies in [18, 19] conducted similar linear stability analysis in the presence of fresh gases flow and it is observed that the flow against the flame propagation results in a larger growth rate than the one predicted by Darrieus-Landau theory, while a flow following the flame propagation direction leads to a smaller growth rate. However, the validation of the Joulin-Sivashinsky model in capturing confinement effects on free flame propagation through comparison with 3D cases is still required.

Fernandez et al. [20–22] simplified the problem to a quasi-2D form using Darcy's law to model the momentum losses of an equidiffusive flame freely propagating through a Hele-Shaw burner. Simulations in [22] have shown that this quasi-2D approach accurately captures the confinement effects observed in 3D simulations in the limit $h/\delta_T \to 0$. However, for channel widths exceeding one thermal flame thickness, it overestimates the cusp size. Moreover, as the channel width increases and the flame front becomes asymmetric between the walls, the flame curvature in the normal direction significantly affects the global propagation speed. Despite these findings, a detailed analysis of the flame structure is still required to understand the interactions between different curvature components and their impact on flame dynamics.

Moreover, the confinement effects on thermodiffusive instability are rarely explored. Numerical studies by Kang et al. [16] found that DL and ST instabilities favor the formation of large scale cells through the merging process, while TD instability enhances the cell splitting mechanism and results in smaller cellular structure. The global flame speed essentially depends on the interaction of these instabilities. On the other hand, the Lewis effect on flame front curvature is extensively explored for lean hydrogen/air mixtures [23–25]. It has been found that the thermodiffusive instability

strengthens local reaction and influences flame global speed. It would be interesting to study the Lewis effect on flame curvature between walls and the impact on global dynamics, as a stable asymmetric flame front shape can be established in narrow channels for premixed flames with smaller than unity Lewis number [26–28]. Studies in [28] also explored the thermodiffusive instability of flames propagating in a Poiseuille shear flow through 3D simulations, and observed that the flame front configuration between walls and along the transverse direction at various channel widths are influenced by the flow rate with $Le < 1$. Yet for freely propagating flames, a detailed study of the interaction between the normal and transverse flame configurations is still needed.

In this study, we investigate the effect of confinement on premixed flames freely propagating in narrow channels using compressible simulations. In addition to conducting 3D and 2D direct numerical simulations (DNS), we extend Joulin-Sivashinsky model within the compressible Navier-Stokes equations to incorporate wall confinement effects and compare it against 3D simulations at various channel widths. The interaction of hydrodynamic and thermodiffusive instabilities is then investigated. Furthermore, we analyze flame curvature in both the transverse and normal directions in 3D simulations by comparing them with 2D simulations.

4. General formulation

A one-step irreversible global reaction model is applied here, with the reaction rate governed by the Arrhenius-type kinetic model $F + O \longrightarrow P$, where F and O denote respectively the fuel and oxidizer, and P is the products. Here a lean mixture is assumed, hence the oxidizer mass fraction remains approximately constant, as explained in [22]. The amount of fuel consumed per unit volume and per unit time is given by $\Omega = B\rho^2 Y \exp(-E/R_g T)$, where the B is the pre-exponential factor, ρ is the mixture density, Y is the fuel mass fraction, T the temperature, R_g the universal gas constant, and $E = \beta R T_b^2/(T_b - T_u)$ is the overall activation energy with β the Zeldovich number and subscripts u and b for the unburnt and burnt gas states in one-dimensional planar flame, respectively. Gases are assumed as ideal gas, with a constant expansion ratio $q = \rho_u/\rho_b = 6$ with $\rho_u = 1.277\,\mathrm{kg/m^3}$, and a constant Schmidt number $Sc = 0.7$, and two Lewis numbers studied: $Le = 1$ and $Le = 0.5$.

The Arrhenius parameters are then chosen as to obtain the desired Lewis number, planar flame velocity S_L, thermal flame thicknesses ($\delta_T = (T_b - T_u)/\max(\nabla T)$), and diffusive flame thicknesses ($\delta_D = D_{th}/S_L$). D_{th} is the

thermal diffusivity. The values of remaining characteristic parameters of the two flames at 1D planar regime are shown in Table 1. The parameters are carefully chosen to reflect practical significance and the flame thickness and speed with units are the real physical quantities and are used directly in the simulations. It is important to note that the primary objective of the present study is not to perform a direct comparison between the two mixtures, and therefore, it is not necessary for all parameters to be identical.

Table 1: Characteristic parameters of two flames

Parameters	Le	β	δ_D	δ_T	S_L
	[−]	[−]	[mm]	[mm]	[m/s]
Flame_1	1	10	0.1	0.43	1
Flame_05	0.5	14	0.128	0.5	0.78

The mass, momentum, energy and species equations are solved under conservative form. The simulation is carried out in the reference frame attached to the flame moving at the flame consumption rate $\mathbf{U}_{ref} = (u_{ref},\ 0,\ 0)$, with $u_{ref} = S_c$ and S_c defined as

$$S_c = -\frac{1}{\rho_u Y_{F,u} h} \int_0^{L_x} \int_0^{L_y} \int_0^{h} \dot{\omega}_F \mathrm{d}x\mathrm{d}y\mathrm{d}z \tag{1}$$

where Y_F is the fuel mass fraction, and $\dot{\omega}_F$ is the fuel reaction rate. The mass and momentum equations are then in the following forms:

$$\begin{aligned} &\frac{\partial \rho}{\partial t} + \nabla \cdot [\rho(\mathbf{u} - \mathbf{U}_{ref})] = 0 \\ &\frac{\partial \rho \mathbf{u}}{\partial t} + \nabla \cdot [\rho \mathbf{u}(\mathbf{u} - \mathbf{U}_{ref})] = -\nabla p + \nabla \cdot \Gamma \end{aligned} \tag{2}$$

where $\mathbf{u}$ is the velocity in the laboratory reference, p is the pressure, and Γ is the viscous tensor defined as

$$\Gamma = \mu\{(\nabla \mathbf{u} + (\nabla \mathbf{u})^T) - \frac{2}{3}(\nabla \cdot \mathbf{u})\mathrm{I}\} \tag{3}$$

with I representing the identity matrix. Each component in Γ is then in form of $\tau_{ij} = \mu(\frac{\partial u_i}{\partial x_j} + \frac{\partial u_j}{\partial x_i}) - \frac{2}{3}\delta_{ij}\nabla \cdot \mathbf{u}$. The conservation of species is considered as:

$$\frac{\partial \rho Y_F}{\partial t} + \nabla \cdot [\rho(\mathbf{u} - \mathbf{U}_{ref})Y_F] = \nabla \cdot (\rho D_F \nabla Y_F) + \dot{\omega}_F \tag{4}$$

where Y_F is the mass fraction of the fuel. The diffusion term is evaluated through Fickian approximation. Naturally we have $Y_P = 1 - Y_F$ for the product. D_F stands for fuel's mass diffusion coefficient, and $\dot{\omega}_F$ is its reaction rate. The energy conservation is originally calculated in the form of total energy (E_t) in our Lattice-Boltzmann based solver ProLB [29]. The detailed formulation is provided in Appendix A. However, it can also be expressed in other forms such as enthalpy and temperature. Here for the sake of simplicity, we give the formulation in the form of temperature (T), as follows:

$$\rho C_P[\frac{\partial T}{\partial t} + (\mathbf{u} - \mathbf{U_{ref}}) \cdot \nabla T] = \frac{Dp}{Dt} + \nabla \cdot (\lambda \nabla T) + \dot{\omega}_T, \tag{5}$$

with the reaction term $\dot{\omega}_T = (h_P - h_F)\dot{\omega}_F$ and the calculation of species enthalpy h_k ($k \in \{F, P\}$) is provided in Appendix B. λ is the thermal conductivity and $\lambda = \frac{\mu C_p}{Pr}$ with μ the dynamic viscosity following the temperature power-law $\mu = \mu_0(\frac{T}{T_0})^{0.7}$. T_0 the reference temperature and $T_0 = 298.15\,\mathrm{K}$. It is noteworthy that the comparison in [22] between constant or temperature-dependent viscosity has highlighted the importance of variable viscosity on global flame speed for narrow channel widths. Pr is the constant Prandtl number. Ideal gas equation of state $\frac{\rho RT}{W} = p$ is applied for thermodynamic closure with W the mean molecular weight.

In two-dimensional simulations of the front-view plane, vectors in Eqs. 2, 4, and 5 only have xy plane components. However, the effect of confinement on the wall yields momentum losses, and the ST instability would strengthen the instability, as studied in [1, 8, 16, 17, 22, 30]. Additional terms should be added to consider this effect. Here the momentum loss is included in the form of viscous force $\mathcal{F} = (\partial\tau_{zx}/\partial z,\ \partial\tau_{zy}/\partial z)$, and added to the momentum equation:

$$\begin{aligned}\frac{\partial \rho(\bar{\mathbf{u}} - \mathbf{U}_{ref})}{\partial t} + \nabla \cdot [\rho\bar{\mathbf{u}}(\bar{\mathbf{u}} - \mathbf{U}_{ref})] = -\nabla p + \\ \nabla \cdot \Gamma^{2D} + \mathcal{F},\end{aligned} \tag{6}$$

where the viscous tensor Γ^{2D} is also defined as in Eq. 3 including only xy plane components. τ_{zx} and τ_{zy} defined as follows:

$$\begin{aligned}\tau_{zx} &= \mu\{\frac{\partial(u_x - u_{ref})}{\partial z} + \frac{\partial u_z}{\partial x}\} \\ \tau_{zy} &= \mu\{\frac{\partial u_y}{\partial z} + \frac{\partial u_z}{\partial y}\}.\end{aligned} \tag{7}$$

with u_x and u_y representing the x and y components of velocity vector, and the second terms on the right hand side ($\frac{\partial u_z}{\partial x}$ and $\frac{\partial u_z}{\partial y}$) negligible. The

velocity field here is modeled by the Poiseuille flow assumption:

$$\mathbf{u} = -6\bar{\mathbf{u}}(\frac{z^2}{h^2} - \frac{z}{h}) \tag{8}$$

where $\bar{\mathbf{u}} = \bar{\mathbf{u}}_{x,y}$ is the flow velocity averaged along z direction. So we have

$$\begin{aligned} \frac{\partial \tau_{zx}}{\partial z} &= \mu \frac{\partial^2 u_x}{\partial z^2} = -\mu \frac{12\bar{u}_x}{h^2} \\ \frac{\partial \tau_{zy}}{\partial z} &= \mu \frac{\partial^2 u_y}{\partial z^2} = -\mu \frac{12\bar{u}_y}{h^2} \end{aligned} \tag{9}$$

Applying this assumption can include the viscous friction term in the momentum equation without solving the flow in z direction. After adding this friction force, the momentum equation becomes:

$$\begin{aligned} \frac{\partial \rho(\bar{\mathbf{u}} - \mathbf{U}_{ref})}{\partial t} + \nabla \cdot [\rho \bar{\mathbf{u}}(\bar{\mathbf{u}} - \mathbf{U}_{ref})] = -\nabla p + \\ \nabla \cdot \Gamma^{2D} + f\bar{\mathbf{u}} \end{aligned} \tag{10}$$

where $f = \frac{-12\mu}{h^2}$. This formulation is hereafter termed the 2D+ simulation, whereas the two-dimensional simulation without this body force term will be denoted as pure 2D simulation. Note that the 2D+ simulations are slightly different from Joulin and Sivashinsky Euler-Darcy formulation [1], which includes the friction term but neglects Γ^{2D} to simplify the theoretical calculations.

5. Numerical setup

A Hele-Shaw burner with two open ends is used to study the propagation of a premixed laminar flame while minimizing acoustic perturbations. The top ($z = h$) and bottom walls ($z = 0$) are set as adiabatic, no-slip boundaries. A constant pressure outlet at 1 bar is applied on the burnt side, formulated as

$$x \longrightarrow -\infty : \frac{\partial \mathbf{u}}{\partial x} = \frac{\partial T}{\partial x} = \frac{\partial Y_k}{\partial x} = 0. \tag{11}$$

A non-reflecting boundary condition is applied on the fresh side (see Table 9.4: B2 in [31]) to simulate an infinitely long domain. The domain length is set to twice the width to avoid effects from the open ends. Periodic boundary conditions are applied along the transverse sides. A schematic of the configuration is shown in Fig. 1.

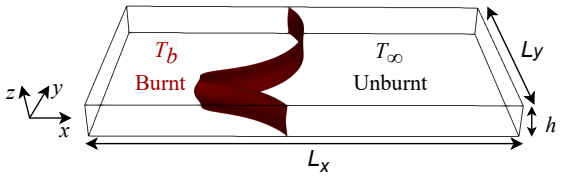

Figure 1: Configuration sketch of curved flame propagating between two walls.

The domain is initially filled with a premixed mixture at a temperature of $T_\infty = 300\,\mathrm{K}$ and pressure $p = 1\,\mathrm{bar}$. The initial condition consists of an initially planar flame, perturbed by a sinusoidal perturbation in the xy plane, with an amplitude $A = 0.4\delta_T$. Additionally, for 3D cases, a tilted planar flame is set in the xz plane to trigger potential asymmetric flame solutions. The mass, momentum, energy and species equations are solved under conservative form using the Lattice-Boltzmann solver ProLB [29, 32–34]. For a detailed derivation of Lattice-Boltzmann methods (LBM), the reader is referred to [34]. Structural mesh resolution of $\Delta x = 0.1\delta_T$ is chosen to resolve the flame. A finer mesh with $\Delta x = 2 \times 10^{-5}\,\mathrm{m}$ is used for the smallest channel width for Flame_1 to capture the flame dynamics between walls, while for the smallest channel width for Flame_05, a resolution of $\Delta x = 10^{-5}\,\mathrm{m}$ is chosen, which will be explained in Section 6.2. The mesh resolutions in the present study show numerical convergence.

6. Results and analysis

In Section 6.1 the capability of 2D+ simulation to recover the momentum loss is analyzed using Flame_1. Section 6.2 investigates the effect of interaction between hydrodynamic and thermodiffusive instabilities using Flame_05.

6.1. 2D+ simulation validation

According to [22] where Flame_1 is applied, there is a critical transverse domain size $\hat{L}_y$ (around $20\delta_T$) above which the flame front would exhibit an unsteady oscillatory behavior. Therefore, a 3D computational domain size of $L_y = 5.7\,\mathrm{mm}$ is chosen here to obtain a steady one-cusp structure for Flame_1. The domain length is chosen as $L_x \approx 2L_y$ and different channel widths are set.

6.1.1. Momentum loss

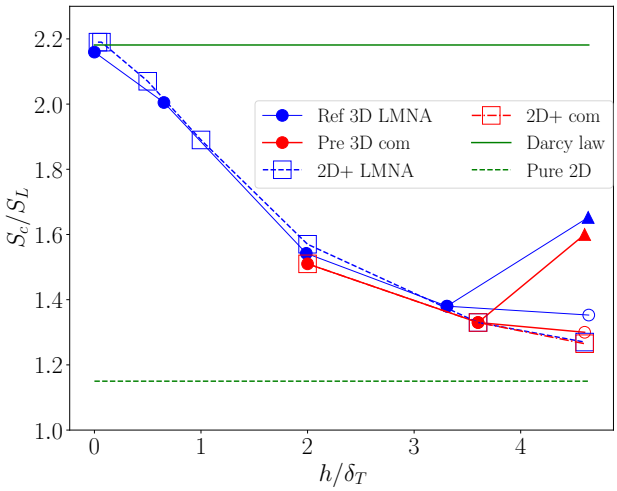

Figure 2: Flame_1, the variation of consumption speed with channel width. Blue circles and triangles represent results from 3D simulations in reference [22], while red circles and triangles correspond to the present 3D simulations. In both studies, solid circles indicate stable, symmetric flame shapes between the walls, while for channel widths h greater than a critical value, stable solutions with asymmetric flame shapes are shown as solid triangles and unstable symmetric solutions—obtained by imposing symmetry boundary conditions as done in [22]—are represented by hollow circles. Hollow squares stand for the present 2D+ simulations, with colors blue and red standing for fully-compressible and LMNA formulations. Green dashed and solid lines representing results from pure 2D simulation and reference [22] using Darcy's law, respectively.

The variation in flame consumption speed with channel width (h ranging from $0.033\delta_T$ to $4.6\delta_T$) is shown in Fig. 2. All values are derived from steady-state solutions. In addition to both 3D and 2D+ cases with the numerical setup described in Section 5, additional 2D+ simulations are carried out with low-Mach number approximation (LMNA) to solve pressure-velocity coupling in order to ensure mass conservation, and the same closed-inlet boundary condition as in [22] to enable comparisons (3D simulations results from [22] are referred as 3D reference), given that for ultra narrow channel widths ($h \leq 1\delta_T$ in the present case), the significant pressure increase on the flame front affects the reaction and the flow with fully compressible codes. In the figure, results with LMNA are represented by blue color, while red color represents fully compressible codes described in Section 5. Compared to 3D cases, the consumption speed is underestimated in the pure 2D case (green dashed line); in contrast, Darcy's law (green solid line) overestimates

the consumption speed except for $h \to 0$, as discussed in [22].

The comparison between the 3D reference, the present 3D and 2D+ simulations is divided into three parts:

- $h \leq \delta_T$
  A strong agreement is observed for $h \leq \delta_T$ between the 3D reference (blue circles) and the present 2D+ model (blue squares). The flame consumption speed increases as the channel width decreases and the Saffman-Taylor instability is enhanced. Moreover, in the limit $h/\delta_T \to 0$, the flame speed predicted by Darcy's law is recovered by the present 2D+ simulation. It should be mentioned that for this range of h, LMNA and the same closed-inlet boundary condition as in reference [22] are necessarily activated to enable the comparison.

- $\delta_T < h \leq 3.6\delta_T$
  For this range of h, the 2D+ simulation (squares) also accurately reproduces the 3D flame consumption speed (circles). Furthermore, the difference between 2D+/reference 3D cases using LMNA and closed-inlet boundary condition (blue squares/circles) and 2D+/3D cases using fully compressible codes and open inlet (red squares/circles) is negligible. Hereafter, we only discuss results with fully compressible codes and open-inlet end as in Section 5. The temporal evolution of flame consumption speeds for 3D and 2D+ cases is provided in Fig. 3 to highlight the good agreement between 3D and 2D+ simulations for symmetric cases.

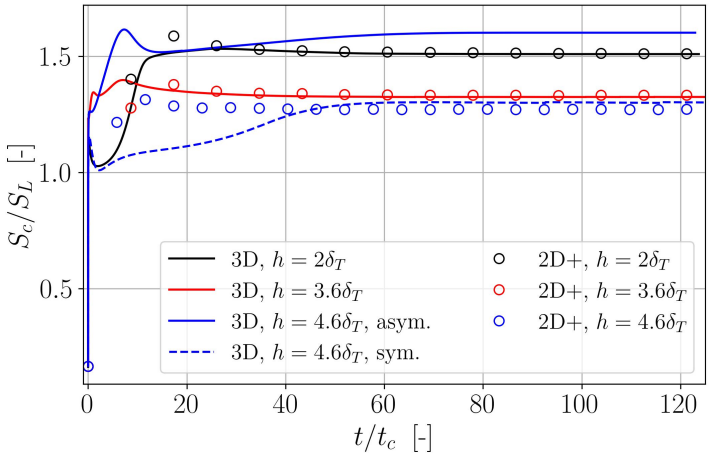

Figure 3: Flame_1, evolution of flame consumption speed with time.

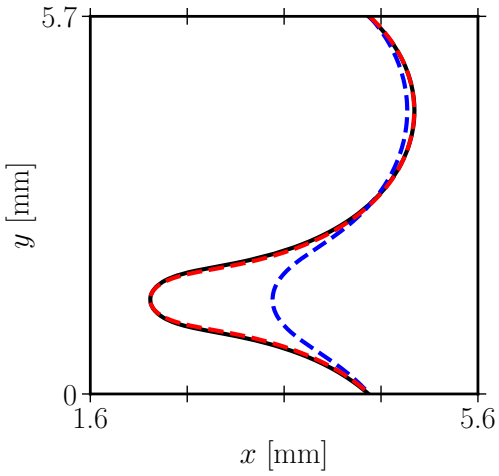

Figure 4: Flame_1, with $h = 2\delta_T$, isocontours of $c = 0.8$ with black curve standing for 3D case in the plane $z = \frac{1}{2}h$, blue curve for pure 2D simulation and red curve for 2D+ simulation.

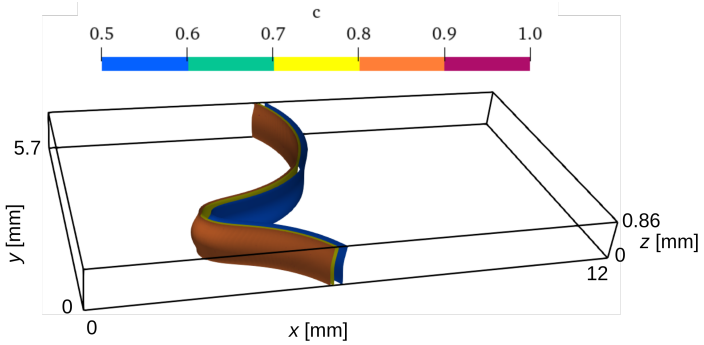

Figure 5: Flame_1, with $h = 2\delta_T$, isocontours of $c = 0.5$, $c = 0.8$, and $c = 0.9$.

Given the unity Lewis number, the consumption speed is solely due to the flame surface increment. Figure 4 illustrates the flame front morphology represented by isocontours of progress variable $c = 0.8$ with $c = 1 - Y_F$ for a channel width $h = 2\delta_T$. The black curve standing for 3D case in the plane $z = \frac{1}{2}h$, while blue and red curves represent the pure 2D simulation and the 2D+ simulation, respectively. Compared to the pure 2D simulation, the friction force contributes to the elongation of the cusp [8], yielding a larger cusp. On the other hand, the flame front between walls is slightly curved and symmetric, yielding negligible contribution to the global surface increment, as shown in in Fig. 5, which presents the isosurfaces at $c = 0.5,\ 0.8$ and 0.9 from the left to the right. Overall, with the increase of channel width, the consumption speeds from both the 3D and 2D+ simulations decrease and converge towards the values from pure 2D simulations as the confinement effect diminishes.

- $h = 4.6\delta_T$

  However, for $h = 4.6\delta_T$, the 3D case yields a stable asymmetric solution which exhibits an increase in consumption speed whereas the 2D+ simulation keeps decreasing. The temporal evolution of Sc/S_L is shown in Fig. 3. This contrast is due to the flame losing its symmetry around the central plane of the channel, which further enhances the consumption speed. The unstable symmetric solution has also been investigated by imposing symmetric boundary in the central plane between walls, as has been done in [22]. The consumption speed of the forced symmetric solution closely matches that predicted by the 2D+ simulation, confirming that the 2D+ model can accurately reproduce the 3D results when the flame is symmetric between the walls.

  Figure 6 illustrates the isocontours of progress variable at $c = 0.5$, 0.8 and 0.9 for forced symmetric and asymmetric solutions with $h = 4.6\delta_T$ in 3D simulation. As a reference, in the forced symmetric case, the flame front between walls is slightly curved and symmetric (see Fig. 6a), whereas the stable asymmetric solution (see Fig. 6b) is highly curved between walls, yielding a larger flame front surface compared to forced symmetric one. Additionally, the cusp sizes vary significantly along the normal direction, implying the interaction between flame curvatures in transverse and normal directions. Together with Fig. 5, it is noteworthy that for each case, there is no observable difference between different isocontours. To analyze the sensibility of the flame front surface to choices of isosurface, Fig. 7 shows the variation of flame

front surface increment A_f/A_0 with the isosurface c for the case with $h = 2\delta_T$ and $h = 4.6\delta_T$. A_0 is the domain section surface $A_0 \equiv L_y \times h$ and the global flame front surface A_f is calculated by

$$A_f = \int_V \sum(\mathbf{x}, t)\mathrm{dV} \tag{12}$$

with the flame surface density (FSD) representing the local, instantaneous surface area of an isosurface per unit volume. Beyond studies focusing on its estimation [35] and its role in turbulent combustion [36–39], other research has employed laminar flame data and FSD formulations to estimate the instantaneous flame surface area [40]. As done in [41], the flame surface density at an isosurface at $c(x, t) = c_0$ can be calculated as the product of the magnitude of ∇c and the "fine gained" PDF:

$$\sum(\mathbf{x}, t) = |\nabla c|\delta(c - c_0), \tag{13}$$

where δ is the Dirac delta function. It is observed that for both cases the flame surface increment is insensible to the c value, as expected.

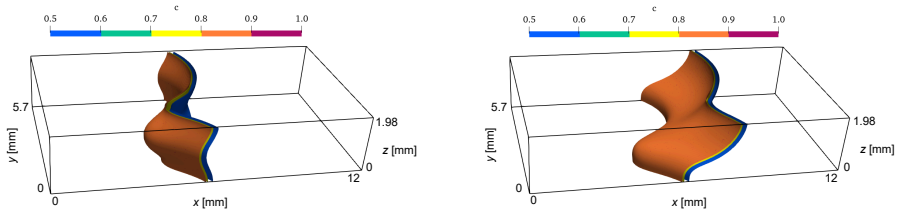

(a) Forced symmetric solution

(b) Asymmetric solution

Figure 6: Flame_1: for $h = 4.6\delta_T$, isocontours of $c = 0.5$, $c = 0.8$, and $c = 0.9$.

6.1.2. Flame curvature interaction

This section investigates the interaction of flame front curvature in both transverse and normal directions for $h = 4.6\delta_T$, where the flame front between walls is asymmetric.

From left to right, the three figures in Fig. 8 illustrate the isocontours of $c = 0.8$ in the plane $z = \frac{1}{3}h$, $z = \frac{1}{2}h$, and $z = \frac{2}{3}h$ for $h = 4.6\delta_T$, in comparison with pure 2D simulation and 2D+ simulations. It is observed that the cusp size varies with the z position. While the 2D+ simulation

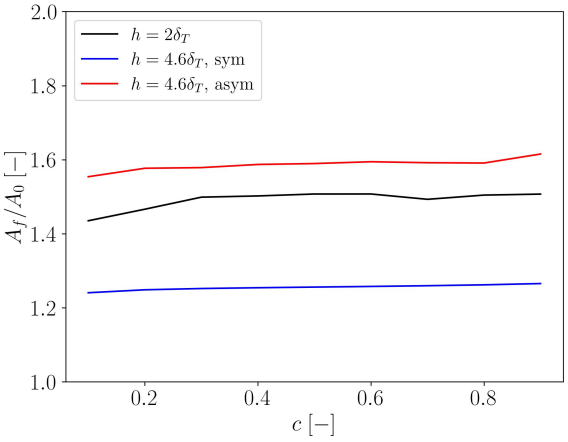

Figure 7: Flame_1, sensitivity of flame front surface increment A_f/A_0 to isosurface c.

closely matches the 3D case at $z = \frac{1}{3}h$, it overestimates the cusp size at planes $z = \frac{1}{2}h$ and $z = \frac{2}{3}h$. Pure 2D simulation, on the other hand, aligns well with the 3D case at $z = \frac{1}{2}h$. This variation in cusp size in the 3D case results from the asymmetric flame front morphology between walls. Overall, in the xy plane, the cusp near the bottom wall is more elongated than the one near the top wall, as the flame front between walls is concave toward fresh gases near the bottom wall and forms an elliptic concave topology.

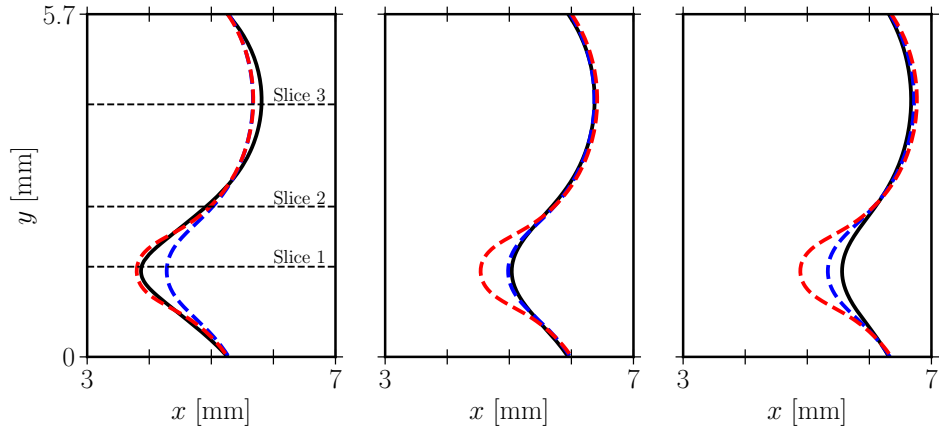

Figure 8: Flame_1, for $h = 4.6\delta_T$, isocontours of $c = 0.8$, with black curves standing for 3D case in the plane xy, blue curves for pure 2D simulation and red curves for 2D+ simulation. From left to right: plane $z = \frac{1}{3}h$; $z = \frac{1}{2}h$; $z = \frac{2}{3}h$.

To better assess the interaction between flame topology in the xy and xz planes, a 2D configuration between walls is also set, as shown in Fig. 9. The boundary conditions in the longitudinal and normal directions are set the same as in the 3D configuration. A steady flame front is established using the same L_x and h as in the 3D case.

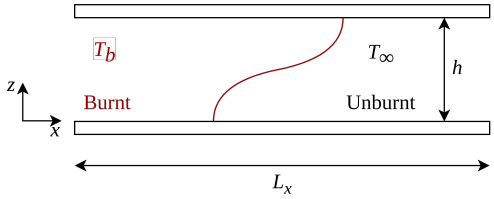

Figure 9: 2D configuration sketch between walls.

Figure 10 compares the flame front shape between walls at different y positions with the steady solution obtained from the 2D configuration in Fig. 9. It is observed that while flame fronts between walls are all asymmetric at different y positions, the extent of elongation varies depending on the location relative to the cusp and tip in the xy plane. In Fig. 10a, which compares the contours at plane $y = 1.5\,\text{mm}$ (Slice 1 annotated in Fig. 8) with the solution from the 2D simulation between walls, the flame front exhibits a longer elongation due to the emergence of a cusp in the xy plane. In contrast, at the plane $y = 4.2\,\text{mm}$ (Slice 3 annotated in Fig. 8) corresponding to the tip in the xy plane, the elongation is shorter than in the 2D simulation, see Fig. 10c. Between the two extremes, at $y = 2.5\,\text{mm}$ (Slice 2 annotated in Fig. 8), the flame fronts in the 3D slice and the 2D simulation between walls are approximately the same, as depicted in Fig. 10b. These observations indicate that the interaction between flame front curvature in the transverse and normal directions significantly influences the local flame morphology.

6.1.3. Flame curvature between walls

For further insight into the flame curvature between walls, slices along the planes xz with a width of $2\Delta x$ are extracted from the 3D case. The flame surface increment is calculated as A_f/A_0, $A_0 = h \times 2\Delta x$ the slices section surface from the yz plane, and A_f the flame front surface of each slice as defined in Eq. 12. Additionally, to separate the stretch due to the curvature in the plane xy, $A_{f,xz}$ is calculated considering only components

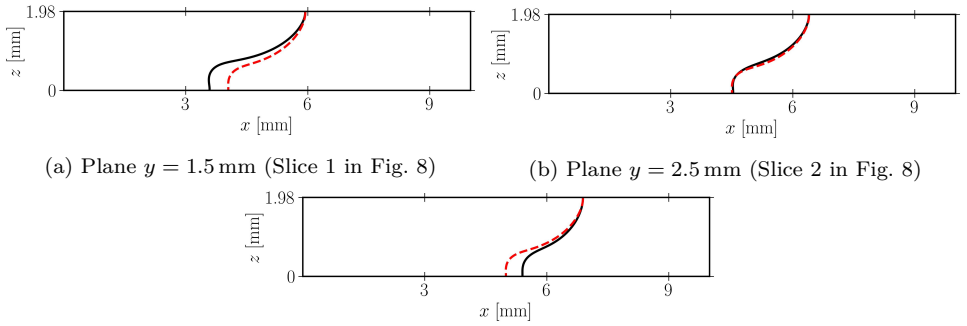

(a) Plane $y = 1.5\,\text{mm}$ (Slice 1 in Fig. 8)

(b) Plane $y = 2.5\,\text{mm}$ (Slice 2 in Fig. 8)

(c) Plane $y = 4.2\,\text{mm}$ (Slice 3 in Fig. 8)

Figure 10: Flame_1, comparison of flame front contours at $c = 0.8$ between 2D simulation between walls (red curve) and 3D slice (black curve) in planes $y = 1.5\,\text{mm}$ (a), $y = 2.5\,\text{mm}$ (b), $y = 4.2\,\text{mm}$ (c).

in the plane xz of ∇c:

$$A_{f,xz} = \int_V \sum(\mathbf{x}, t)_{xz} \text{dV} \tag{14}$$

with

$$\sum(\mathbf{x}, t)_{xz} = |\{\nabla c\}_{xz}|\delta(c - c_0). \tag{15}$$

Both A_f and $A_{f,xz}$ are calculated at the slice isosurface $c = 0.8$. Their probability distribution function is shown in Fig. 11. For both A_f and $A_{f,xz}$, the first peak appears around $A_f/A_0 = 1.35$, corresponding to the region near the plane $y = 4.2\,\text{mm}$, where is located the flame front tip in the xy plane. The difference in the second peak ($\{A_f/A_0\}_{3D} = 1.78$ vs. $\{A_{f,xz}/A_0\}_{3D} = 1.68$) arises from the stretch effect around the cusp in the xy plane. A wider range of A_f/A_0 also indicates this strong flame stretch. The average flame surface increment between walls in the 3D case $\{ave(A_{f,xz}/A_0)\}_{3D} = 1.46$ is close to the 2D simulation between walls ($\{A_f/A_0\}_{2D} = 1.49$) (represented by the blue dashed line in the figure), while the average value of A_f/A_0 overestimates the flame surface increment due to the additional stretch effect in the xy plane.

The sensibility of A_f/A_0 of slices to choices of c is also analyzed, as shown in Fig. 12. All three flame surface increments are approximately constant despite different c. Moreover, $A_{f,xz}/A_0$ remains close to the value from the 2D configuration.

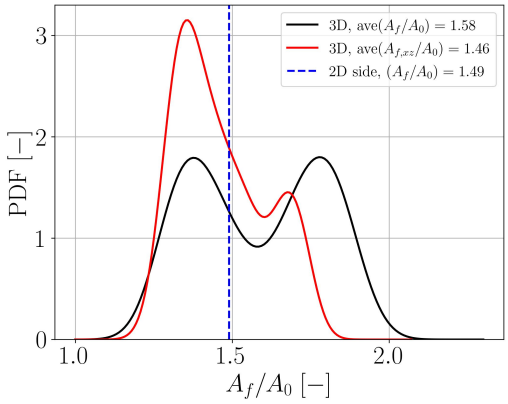

Figure 11: Flame_1, probability distribution of flame front surface increment A_f/A_0 of slices with $h = 4.6\delta_T$ and $L_y = 5.7\,\text{mm}$.

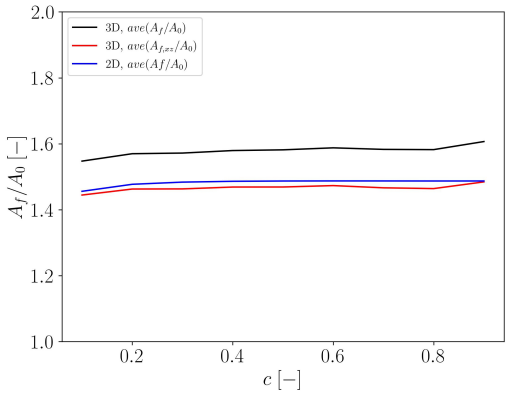

Figure 12: Flame_1, sensitivity of flame front surface increment A_f/A_0 of slices to iso-surface c for $h = 4.6\delta_T$.

6.2. Interaction between hydrodynamic and thermodiffusive instabilities

The aforementioned sections focus solely on hydrodynamic instabilities (ST and DL instabilities). In this section, the confinement effect on Flame_05, which also exhibits intrinsic thermodiffusive instability, will be studied. According to 2D studies, the critical channel width for Flame_05 to sustain a stable asymmetric flame is $h_c = 0.8\delta_T$. To investigate the flame structure and the interaction of intrinsic instabilities with the asymmetric flame between walls, two 3D cases are considered. Both have a transverse width of $L_y = 7.2\delta_T$.

6.2.1. Flame structure in 3D

Two cases with different channel widths ($h = 1.2\delta_T$ and $h = 2\delta_T$) are set and initialized both with sinusoidally perturbed planar flames. For both cases, the flame fronts converge to an ultimate steady structure in time, which consists of three cusps, as depicted by the isosurface $c = 0.8$ in Fig. 13. In the steady state, the consumption speeds for the two cases: $h = 1.2\delta_T$ and $h = 2\delta_T$, are listed in Table 2, represented by S_c/S_L. The increase in the flame speed mainly comes from: (1) likewise, both the curvature in the transverse direction and between walls in 3D cases result in a significant increase in flame surface and consequently the consumption speed, represented by the flame surface increment parameter A_f/A_0; (2) preferential diffusion on the flame front with positive curvature between walls strengthens local reaction rates, evaluated by the amplification factor $I_0 = \{S_c/S_L\}/\{A_f/A_0\}$. The isosurface at $c = 0.8$ is chosen as representative of the flame front, and $A_0 = L_y \times h$. Table 2 also summarizes the values of these parameters of interest for the two cases. As can be observed in Fig. 13, a larger channel width leads to a higher flame front surface increment, whereas the amplification factor decreases, which is related to the flame front positive curvature. Figure 14 presents the PDF results of curvature on the flame front at $c = 0.8$ for the two cases. The curvature is adimensionlized by multiplying by the thermal flame thickness. In addition to a higher positive curvature at the peak probability, a larger positive curvature distribution is also found with smaller channel width, which favors the reactivity owing to the Lewis effect.

This enhancement because of the Lewis effect on curvature is also illustrated in Fig. 13 through the distribution of HRR_{norm} and the curvature κ in the isosurface $c = 0.8$ in 3D simulations. HRR_{norm} is the ratio of heat release rate (HRR) to the value of HRR in 1D planar flame at $c = 0.8$. Figure 13 shows a considerable increase ($\times 100$) in reaction where the flame front is convex toward fresh gases. On the other hand, flame decelerates where the flame front is concave toward fresh gases.

Table 2: Flame_05, the mean value of flame consumption speed S_c/S_L, flame front surface A_f/A_0, and the amplification factor I_0 from 3D cases with channel widths $h = 1.2\delta_T$ and $h = 2\delta_T$.

h/δ_T	S_c/S_L	A_f/A_0	I_0
1.2	6.74	3.19	2.11
2	7.81	4.29	1.82

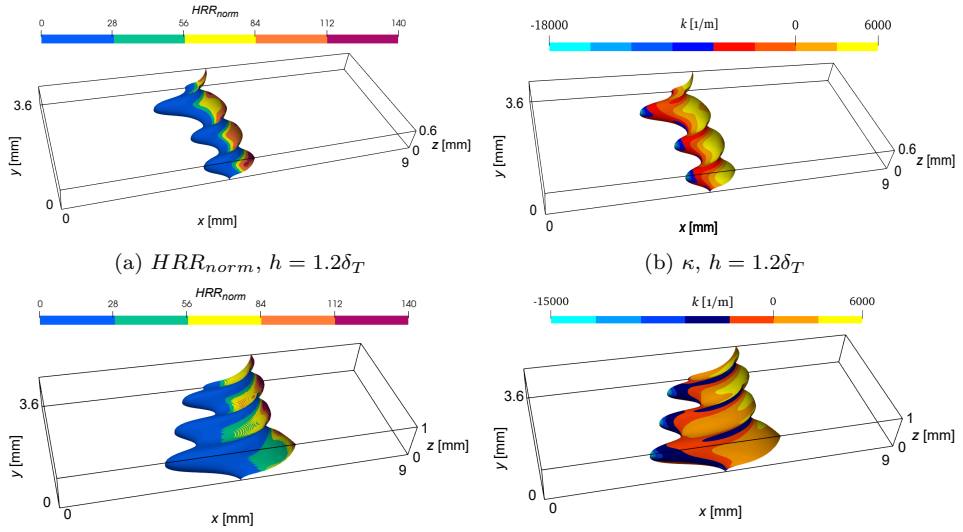

(a) HRR_{norm}, $h = 1.2\delta_T$ (b) κ, $h = 1.2\delta_T$

(c) HRR_{norm}, $h = 2\delta_T$ (d) κ, $h = 2\delta_T$

Figure 13: Flame_05, HRR (HRR_{norm}) and curvature (κ) distribution on isosurface $c = 0.8$.

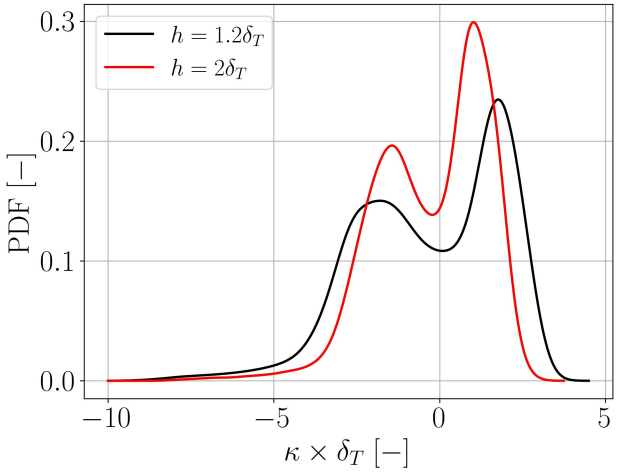

Figure 14: Flame_05, probability distribution of curvature on flame front at isosurface $c = 0.8$.

Figure 15 presents the proportions of negative curvature and positive curvature (black bars) on the flame front, as well as their contributions to the total heat release rate (red bars). For both $h = 1.2\delta_T$ and $h = 2\delta_T$, the

surface ratios of convex and concave regions on the flame front are largely equivalent, while more than 90% HRR comes from the convex part.

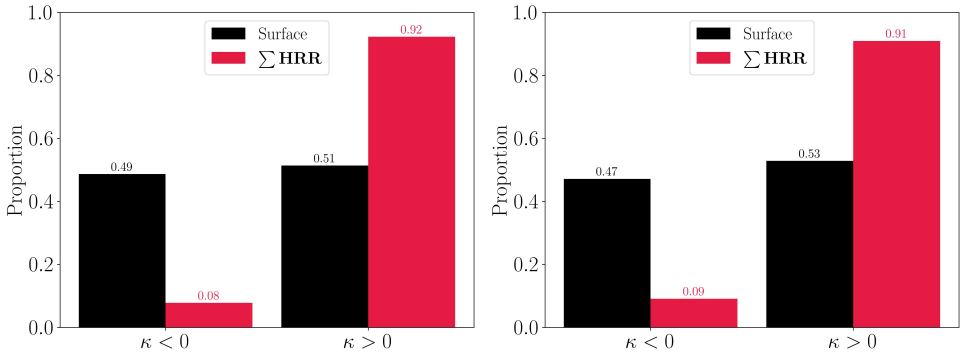

(a) $h = 1.2\delta_T$ (b) $h = 2\delta_T$

Figure 15: Flame_05, the proportions of positive and negative curvature κ and their contribution to total heat release rate HRR with $h = 1.2\delta_T$ (a) and $h = 2\delta_T$ (b).

In the xy plane, the cusp size on the flame front varies along the direction z, similar to the case with Flame_1. The elongation of cusps in the plane xy near the bottom wall is greater than the one near the top wall due to the cusp in the plane xz, which also locates near the bottom wall. The conjunction of these two cusps yields an elliptic concave topology, as discussed in Section 6.1.2, and greatly decreases the reaction. This explains why the region from the bottom wall to $y = \frac{1}{4}h$ has a negligible contribution to HRR.

Moreover, the flame inner structure for the 3D case with $h = 1.2\delta_T$ is analyzed through the norm of progress variable divergence $|\nabla c|$, as shown in Fig. 16a. The maximum of conditional average for the 3D case is around three times higher than the one for 1D planar flame, indicating a much thinner flame. The grid resolution of 10^{-5} m is thus chosen to well resolve the flame inner structure.

Additionally, Fig. 16 distinguishes $|\nabla c|$ with positive and negative curvature by black and red colors, respectively. It is observed that positive curvature drastically increases $|\nabla c|$, i.e. strong convexity of the flame front thins the flame thickness due to the Lewis effect. Figure 16b and c show the distribution of $|\nabla c|$ for $z > \frac{9}{10}h$ and $z < \frac{1}{10}h$, respectively. Given the asymmetric flame front shape between walls (see Fig. 13), which exhibits convexity close to the top wall ($z = h$) and concavity near the bottom wall

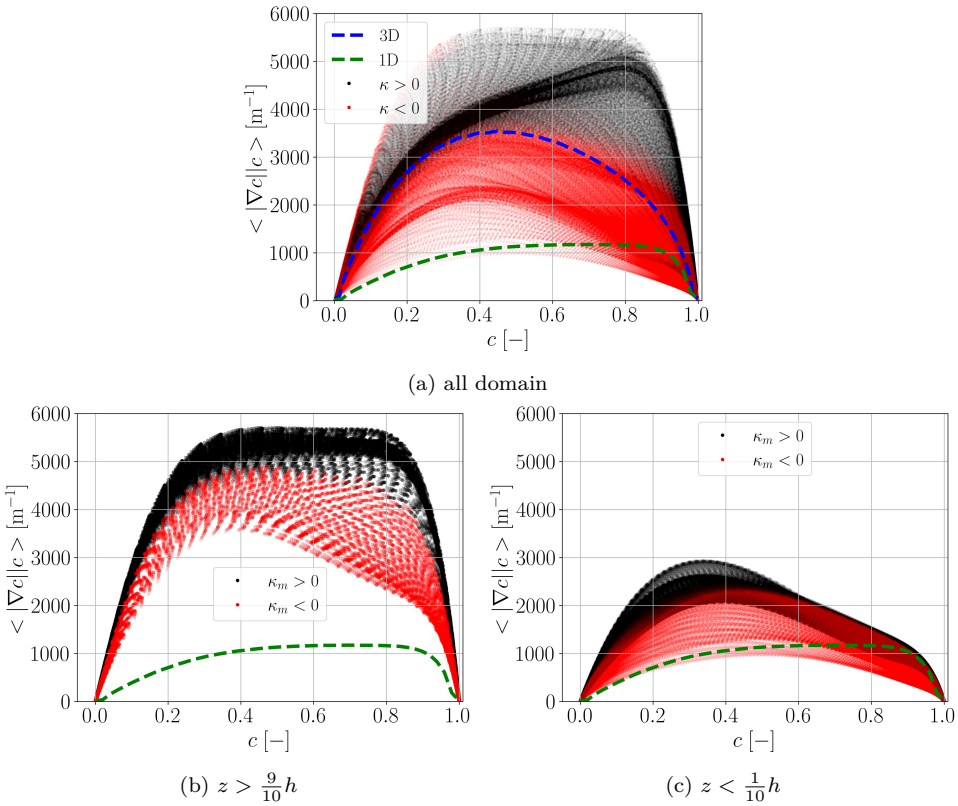

(a) all domain

(b) $z > \frac{9}{10}h$

(c) $z < \frac{1}{10}h$

Figure 16: Flame_05, (a) norm of progress variable divergence $|\nabla c|$ across the entire domain with $h = 1.2\delta_T$, where black and red points indicate positive/negative curvature, respectively. The conditional average is represented by blue (3D) and green (1D) dashed lines. (b) and (c) show $|\nabla c|$ for regions $z > \frac{9}{10}h$ and $z > \frac{9}{10}h$, respectively, with black/red points representing positive/negative curvature in the xy plane.

$(z = 0)$, of interest here is the positive average curvature κ_m, defined as

$$\kappa_m = \nabla \cdot n_{xy},\ n_{xy} = \{\nabla c\}_{xy}/|\{\nabla c\}_{xy}|,$$

where $\{\nabla c\}_{xy}$ only has components in the xy plane. Hence, κ_m represents the flame front convexity in the plane xy. Together with Fig. 16a, it can be observed that convexity in the xz plane dominates the flame inner structure, yielding considerably higher $|\nabla c|$ for $z > \frac{9}{10}h$. This highlights the critical role of asymmetric flame dynamics in confined environments, as they substantially impact the overall flame structure. Furthermore, convexity in the plane xy modulates the amplitude of $|\nabla c|$: positive κ_m leads to higher $|\nabla c|$

compared to negative κ_m.

6.2.2. Flame dynamics between walls

Similar to Section 6.1.2, slices along the planes xz with a width of $2\Delta x$ are extracted from 3D cases to investigate the flame dynamics between walls for Flame_05. The flame surface increment is calculated as A_f/A_0, with A_f the flame front surface calculated at isosurface $c = 0.8$ of each slice, and $A_0 = h \times 2\Delta x$ the slices section surface from the yz plane. Here $c = 0.8$ is chosen as a representation of the flame front. Previous studies reveal that regions with negative curvature have a negligible contribution to the global reaction, and the flame front convexity in the plane xy is consistent as shown in Fig. 13. Besides, the convex part ($\kappa_m > 0$) also contributes more than 90% of the global reaction rate. Of interest here are the slices with positive average curvature κ_m. Hereafter, the star superscript $*$ refers to slices with $\kappa_m > 0$.

The probability distribution function (PDF) of A_f/A_0 is shown in Fig. 17. Taking into account all slices (black curve) results in a higher average flame surface increment between two walls since the flame elongation toward burnt gases for slices with negative κ_m is larger, as explained in Section 6.1.2. The PDF distribution of the flame front surface with positive average κ_m (red curve, termed A_f^*/A_0), however, exhibits one significant maximum around 1.6 for $h = 1.2\delta_T$, which is close to the value from 2D simulation between walls (1.74). Likewise, the flame surface increment without the stretch from the plane xy is also calculated using Eqs. 14 and 15, which exhibits a narrower range and a more significant peak located at $\{ave(A^*_{f,xz}/A_0)\}_{3D} = 1.55$. A similar observation is obtained in Fig. 17b for $h = 2\delta_T$. Likewise, compared to a more homogeneous distribution for all slices, the surface increment of slices with positive κ_m shows a peak around 2, also close to the value 2.12 in the 2D simulation between walls. Without the stretch from the curvature in the plane xy, $\{ave(A^*_{f,xz}/A_0)\}_{3D}$ shows a more significant peak at $\{ave(A^*_{f,xz}/A_0)\}_{3D} = 1.9$.

It should be mentioned that the isosurface area for $Le = 0.5$ is sensitive to the c value (a difference greater than 70% between isosurfaces $c = 0.1$ and $c = 0.9$ in 3D). A sensitivity analysis of the choice of isosurface on the flame front surface is conducted. Figure 18 presents the variation of flame surface increment with the choice of isosurface c on the flame front, from both 3D and 2D configurations. It is observed that for both configurations, A_f/A_0 increases considerably with c. Moreover, all curves exhibit the same variation trends. Besides, the surface increment without the stretch from

the curvature in the plane xy ($\{ave(A^*_{f,xz}/A_0)\}_{3D}$) is close to the value $\{ave(A_f/A_0)\}_{2D}$ from 2D configuration.

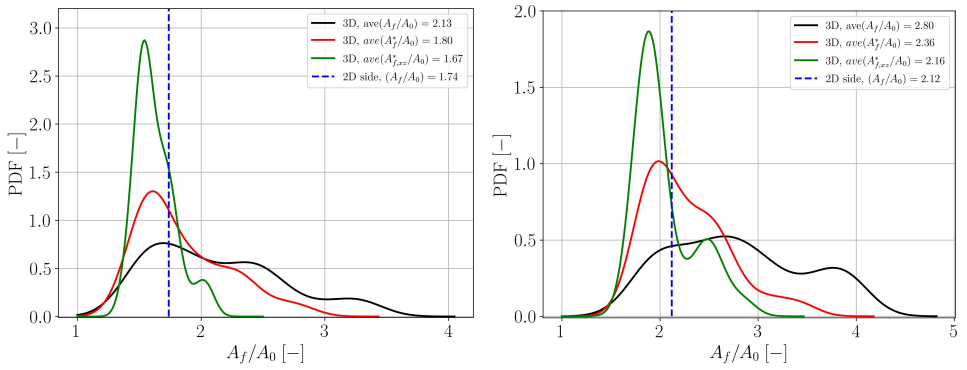

(a) $h = 1.2\delta_T$ (b) $h = 2\delta_T$

Figure 17: Flame_05, probability distribution of flame front surface increment A_f/A_0, with (a) $h = 1.2\delta_T$ and (b) $h = 2\delta_T$.

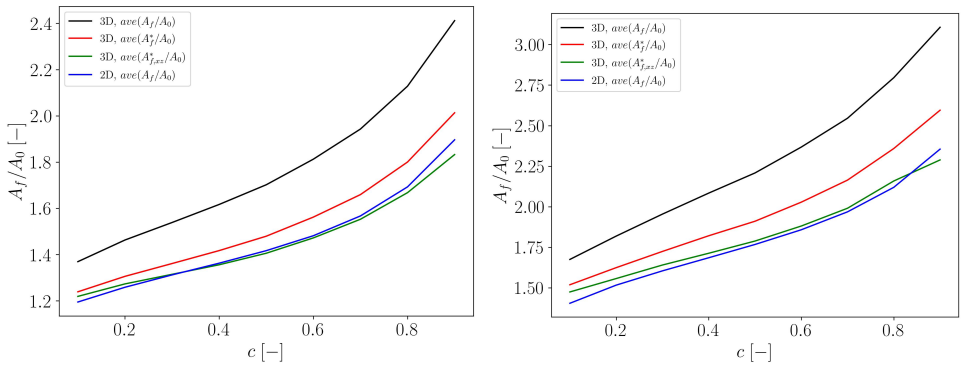

(a) $h = 1.2\delta_T$ (b) $h = 2\delta_T$

Figure 18: Flame_05, sensitivity of flame front surface increment A_f/A_0 of slices to isosurface c.

The correlation of S^*_c/S_L with A^*_f/A_0 (from slices with positive average curvature κ_m) is illustrated in Fig. 19. There is a positive linear correlation between the two parameters, indicating the contribution from flame surface increment to consumption rate. The contribution of the Lewis effect on flame front curvature to reaction rate can be evaluated through the amplification factor $I_0 = S^*_c A_0/S_L A^*_f$. The average value $I_{0,3D-slice}$ for $h = 1.2\delta_T$ is 4.12 with a variance of 0.22. While in the 2D between wall case, the amplification

factor $I_{2D,side}$ is 3.09. The difference comes from the elliptic convex form in the 3D case, where preferential diffusion would further increase the local reaction because of two positive principal curvatures, while in the 2D case there is only one. Likewise, the average amplification factor for 3D slices with $h = 2\delta_T$ is 3.90 with a variance of 0.11, while in the 2D configuration between walls $I_0 = 2.69$.

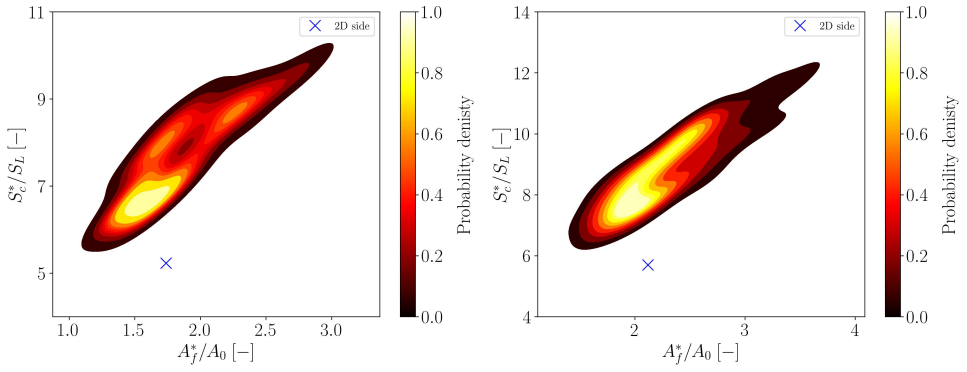

(a) $h = 1.2\delta_T$ (b) $h = 2\delta_T$

Figure 19: Flame_05, joint probability distribution of consumption rate S_c/S_L with flame surface A_f/A_0 for all slices with positive mean curvature, with (a) $h = 1.2\delta_T$ and (b) $h = 2\delta_T$. Blue crosses are from 2D simulations between walls.

The statistical analysis of flame dynamics for 3D slices reveals that acceleration due to both the flame morphology between walls and the Lewis effect can be well depicted by the relation $S_c/S_L = I_0 \times A_f/A_0$. And the value of both the amplification factor and the flame surface increment can be approximately predicted with 2D simulations between walls.

7. Conclusions

In this study, we investigated the effect of wall confinement due to two adiabatic walls on premixed flames freely propagating in narrow channels using compressible simulations. Two lean fuel-air mixtures are considered: one with unity Lewis number $Le = 1$ considering solely hydrodynamic instabilities, and another with $Le = 0.5$ to include the thermodiffusive instability. To evaluate the impact of confinement on flame instability, we conducted 3D numerical simulations (DNS) with varying channel widths and pure 2D simulations in the xy plane (no confinement). Additionally, we extended the

Joulin-Sivashinsky model to incorporate friction due to wall confinement effects into 2D simulations (2D+).

By setting a premixed equidiffusive flame ($Le = 1$), results from 3D simulations show that the confinement effect enhances the hydrodynamic instability and results in a larger single cusp on the flame front in the xy plane, while the impact diminishes as the channel width increases, consistent with previous findings. Moreover, 2D+ model accurately captures the effects of confinement on flame dynamics at various channel widths ans recovers the flame speed, provided that the flame front remains symmetric between the walls. For 3D cases where the flame front shape is asymmetric, the flame curvature in the transverse direction is significantly influenced by strong curvature between walls. Compared to both pure 2D and 2D+ simulations, the 3D simulations exhibit a smaller cusp in the xy plane where forms a convex curvature between walls, while interactions between cusps in two directions lead to larger cusp sizes in the xy plane. These interactions also impact the flame dynamics in the normal direction. Compared to the 2D simulation between walls, the stretch induced from the xy plane alters the flame surface increment between walls, leading to a longer elongation near the flame front cusp and a smaller elongation near the tip in the xy plane. Moreover, by separating the stretch effect from the plane xy, it is found that the flame surface increment between walls is close to that from the 2D configuration.

For $Le = 0.5$, 3D simulations with asymmetric flame shapes between walls are studied. It is found that the Lewis effect amplifies the role of curvature: regions with positive curvature on the flame front mainly contribute to the global reaction. In addition, flame front curvature between walls dominates the flame inner structure and results in significantly thinner thermal flame thickness. Overall, the statistical analysis shows that the flame dynamics between walls are consistent across configurations. Similar to equidiffusive flames, the flame surface increment between walls (without the stretch effect from the xy plane) is close to the value from the 2D configuration between walls. In addition, the acceleration between walls can be well described by the product of the flame front surface increment and the amplification factor, both of which can be predicted by the 2D configuration between walls.

8. Acknowledgments

This research was supported by the ECOSAFE ANR project ANR-21-CE05-0028. Centre de Calcul Intensif d'Aix-Marseille and GENCI-TGCC/CINES

(Grant A0152B11951) are acknowledged for granting access to their high-performance computing resources. Daniel Fernández-Galisteo is gratefully acknowledged for fruitful discussion.

References

[1] G. Joulin, G. Sivashinsky, Influence of momentum and heat losses on the large-scale stability of quasi-2d premixed flames, Combust. Sci. Technol. 98 (1994) 11–23.

[2] G. I. Sivashinsky, Diffusional-thermal theory of cellular flames, Combust. Sci. Technol. 15 (1977) 137–145.

[3] B. DENET, On non-linear instabilities of cellular premixed flames, Combust. Sci. Technol. 92 (1993) 123–144.

[4] B. Denet, P. Haldenwang, A numerical study of premixed flames darrieus-landau instability, Combust. Sci. Technol. 104 (1995) 143–167.

[5] M. Matalon, C. Cui, J. K. Bechtold, Hydrodynamic theory of premixed flames: effects of stoichiometry, variable transport coefficients and arbitrary reaction orders, J. Fluid Mech. 487 (2003) 179–210.

[6] C. Almarcha, B. Denet, J. Quinard, Premixed flames propagating freely in tubes, Combust. Flame 162 (2015) 1225–1233.

[7] H. Thomé, M. Rabaud, V. Hakim, Y. Couder, The saffman–taylor instability: From the linear to the circular geometry, Phys. Fluids A. 1 (1989) 224–240.

[8] S. H. Kang, H. G. Im, S. W. Baek, A computational study of saffman–taylor instability in premixed flames, Combust. Theor. Model. 7 (2003) 343.

[9] D. H. Sharp, An overview of rayleigh-taylor instability, Physica D 12 (1984) 3–18.

[10] P. M. J. TREVELYAN, C. ALMARCHA, A. DE WIT, Buoyancy-driven instabilities of miscible two-layer stratifications in porous media and hele-shaw cells, J. Fluid Mech. 670 (2011) 38–65.

[11] M. Battikh, E. Al Sarraf, B. Radisson, C. Almarcha, B. Denet, Nonlinear dynamics of upward propagating flames, Phys. Rev. E 107 (2023) 065110.

[12] G. Searby, Acoustic instability in premixed flames, Combust. Sci. Technol. 81 (1992) 221–231.

[13] A. Petchenko, V. Bychkov, V. Akkerman, L.-E. Eriksson, Flame–sound interaction in tubes with nonslip walls, Combust. Flame 149 (2007) 418–434.

[14] K. Bhairapurada, B. Denet, P. Boivin, A Lattice-Boltzmann study of premixed flames thermo-acoustic instabilities, Combust. Flame 240 (2022) 112049.

[15] B. Radisson, J. Piketty-Moine, C. Almarcha, Coupling of vibro-acoustic waves with premixed flame, Phys. Rev. Fluids. 4 (2019) 121201.

[16] S. Kang, S.-W. Baek, H. Im, Effects of heat and momentum losses on the stability of premixed flames in a narrow channel, Combust. Theor. Model. 10 (2006) 659–681.

[17] Y. Han, M. Modestov, D. M. Valiev, Effect of momentum and heat losses on the hydrodynamic instability of a premixed equidiffusive flame in a hele–shaw cell, Phys. Fluids 33 (2021).

[18] T. Miroshnichenko, V. Gubernov, S. Minaev, Hydrodynamic instability of premixed flame propagating in narrow planar channel in the presence of gas flow, Combust. Theor. Model. 24 (2020) 362–375.

[19] J. Daou, P. Rajamanickam, Hydrodynamic instabilities of propagating interfaces under darcy's law, Phys. Rev. Fluids. 10 (2025) 013201.

[20] D. Fernández-Galisteo, V. N. Kurdyumov, P. D. Ronney, Analysis of premixed flame propagation between two closely-spaced parallel plates, Combust. Flame 190 (2018) 133–145.

[21] D. Fernández-Galisteo, V. N. Kurdyumov, Impact of the gravity field on stability of premixed flames propagating between two closely spaced parallel plates, Proc. Combust. Inst. 37 (2019) 1937–1943.

[22] D. Fernández-Galisteo, A. Dejoan, J. Melguizo-Gavilanes, V. N. Kurdyumov, A three-dimensional study of the influence of momentum loss on hydrodynamically unstable premixed flames, Proc. Combust. Inst. 39 (2023) 1545–1554.

[23] L. Berger, K. Kleinheinz, A. Attili, H. Pitsch, Characteristic patterns of thermodiffusively unstable premixed lean hydrogen flames, Proc. Combust. Inst. 37 (2019) 1879–1886.

[24] L. Berger, A. Attili, H. Pitsch, Intrinsic instabilities in premixed hydrogen flames: parametric variation of pressure, equivalence ratio, and temperature. part 2 – non-linear regime and flame speed enhancement, Combust. Flame 240 (2022) 111936.

[25] L. Berger, M. Grinberg, B. Jürgens, P. E. Lapenna, F. Creta, A. Attili, H. Pitsch, Flame fingers and interactions of hydrodynamic and thermodiffusive instabilities in laminar lean hydrogen flames, Proc. Combust. Inst. 39 (2023) 1525–1534.

[26] A. Dejoan, C. Jiménez, V. N. Kurdyumov, Critical conditions for non-symmetric flame propagation in narrow channels: Influence of the flow rate, the thermal expansion, the lewis number and heat-losses, Combust. Flame 209 (2019) 430–440.

[27] C. Ziyin, B. Yves, Z. Song, D. Bruno, A. Christophe, B. Pierre, Study on symmetric/asymmetric hydrogen flame shapes in the thickness of a hele-shaw burner, Combust. Flame 277 (2025) 114208.

[28] A. Kelly, P. Rajamanickam, J. Daou, J. R. Landel, Three-dimensional diffusive-thermal instability of flames propagating in a plane poiseuille flow, Proc. Combust. Inst. 40 (2024) 105258.

[29] S. Zhao, K. Bhairapurada, M. Tayyab, R. Mercier, P. Boivin, Lattice-boltzmann modelling of the quiet and unstable preccinsta burner modes, Comput. Fluids. 260 (2023) 105898.

[30] A. Dejoan, Z. Zhou, D. Fernández-Galisteo, P. D. Ronney, V. N. Kurdyumov, Effect of confinement on the propagation patterns of lean hydrogen–air flames, Proc. Combust. Inst. 40 (2024) 105431.

[31] T. Poinsot, D. Veynante, Theoretical and numerical combustion, RT Edwards, Inc., 2005.

[32] M. Tayyab, S. Zhao, Y. Feng, P. Boivin, Hybrid regularized lattice-boltzmann modelling of premixed and non-premixed combustion processes, Combust. Flame 211 (2020) 173–184.

[33] M. Tayyab, S. Zhao, P. Boivin, Lattice-boltzmann modeling of a turbulent bluff-body stabilized flame, Phys. Fluids 33 (2021) 031701.

[34] G. Farag, S. Zhao, T. Coratger, P. Boivin, G. Chiavassa, P. Sagaut, A pressure-based regularized lattice-boltzmann method for the simulation of compressible flows, Phys. Fluids 32 (2020) 066106.

[35] D. Veynante, G. Lodato, P. Domingo, L. Vervisch, E. R. Hawkes, Estimation of three-dimensional flame surface densities from planar images in turbulent premixed combustion, Exp. Fluids 49 (2010) 267–278.

[36] S. Kheirkhah, S. Mohammadnejad, Effects of combustion progress variable and karlovitz number on the scalar dissipation rate of turbulent premixed hydrogen-enriched methane–air flames: An experimental study, Combust. Flame 269 (2024).

[37] S. Mohammadnejad, S. Kheirkhah, Spectral characteristic of a scalar-dissipation-rate-based turbulent burning velocity, Phys. Rev. Fluids 10 (2025) 023201.

[38] L. Berger, A. Attili, H. Pitsch, Synergistic interactions of thermodiffusive instabilities and turbulence in lean hydrogen flames, Combust. Flame 244 (2022) 112254.

[39] L. Berger, A. Attili, M. Gauding, H. Pitsch, Les combustion model for premixed turbulent hydrogen flames with thermodiffusive instabilities: a priori and a posteriori analysis, J. Fluid Mech. 1003 (2025) A33.

[40] X. Wen, L. Berger, L. Cai, A. Parente, H. Pitsch, Thermodiffusively unstable laminar hydrogen flame in a sufficiently large 3d computational domain – part i: Characteristic patterns, Combust. Flame 263 (2024) 113278.

[41] L. Vervisch, E. Bidaux, K. Bray, W. Kollmann, Surface density function in premixed turbulent combustion modeling, similarities between probability density function and flame surface approaches, Phys. Fluids 7 (1995) 2496–2503.

[42] B. McBride, M. Zehe, S. Gordon, Nasa glenn coefficients for calculating thermodynamic properties of individual species (2002).

Appendix A. Energy equation in the form of total energy

The energy conservation equation in terms of total energy is expressed as:

$$\frac{\partial \rho E_t}{\partial t} + \nabla \cdot [\rho(\mathbf{u}-\mathbf{U}_{ref})E_t] = -\nabla \cdot \mathbf{q} + \nabla \cdot [(\Gamma - p\mathrm{I})(\mathbf{u} - \mathbf{U}_{ref})] \tag{A.1}$$

where $E_t \equiv e + \frac{1}{2}(\mathbf{u} - \mathbf{U}_{ref}) \cdot (\mathbf{u} - \mathbf{U}_{ref})$ and e is the internal energy defined as

$$\begin{aligned} e \equiv h - \frac{p}{\rho} &= \sum_k Y_k h_k - \frac{p}{\rho} \\ &= \sum_k Y_k \left(\int_{T_0}^{T} C_{p,k} dT + \Delta h^o_{f,k}\right) - \frac{p}{\rho} \end{aligned} \tag{A.2}$$

with $k \in \{F, P\}$ referring to the fuel (F) and the product (P), $C_{p,k}$ the species heat capacity at constant pressure (NASA polynomials systems for fuel and product are provided in Appendix B), T_0 the reference temperature $T_0 = 298.15\,\mathrm{K}$, and $\Delta h^o_{f,k}$ the species mass formation enthalpy. For the heat energy flux $\mathbf{q}$, we have:

$$\mathbf{q} = -\lambda \nabla T - \rho \sum_k h_k D_k \nabla Y_k \tag{A.3}$$

Appendix B. NASA polynomials for F $\longrightarrow$ P chemistry

The species F and P have different NASA 7 polynomials systems [42] for their thermochemical parameters such as the specific heat and enthalpy. NASA polynomials of both fuel and product are listed in the table below. For $T \leq 1000\,\mathrm{K}$, we have

Parameters	F	P
a_1	3.543	3.543
a_2-a_5	0.0	0.0
a_6	0	$-(T_b - T_u)a_1$
a_7	0	0
a_8	3.543	3.543
a_9-a_{12}	0	0
a_{13}	0	$-(T_b - T_u)a_1$
a_{14}	0	0

Table B.3: NASA polynomials for F $\longrightarrow$ P chemistry.

$$\frac{C_{p,k}}{R} = a_1 + a_2 T + a_3 T^2 + a_4 T^3 + a_5 T^4,$$

and

$$\frac{h_k}{RT} = a_1 + a_2\frac{T}{2} + a_3\frac{T^2}{3} + a_4\frac{T^3}{4} + a_5\frac{T^4}{5} + a_6\frac{1}{T}.$$

Otherwise

$$\frac{C_{p,k}}{R} = a_8 + a_9 T + a_{10}T^2 + a_{11}T^3 + a_{12}T^4,$$

$$\frac{h_k}{RT} = a_8 + a_9\frac{T}{2} + a_{10}\frac{T^2}{3} + a_{11}\frac{T^3}{4} + a_{12}\frac{T^4}{5} + a_{13}\frac{1}{T}.$$